Statistical adaptive sensing by detectors with spectrally overlapping bands

Ünal Sakoğlu, Majeed M. Hayat, J. Scott Tyo, Philip Dowd, Senthil Annamalai, Kalyan T. Posani, and Sanjay Krishna

It has recently been reported that by using a spectral-tuning algorithm, the photocurrents of multiple detectors with spectrally overlapping responsivities can be optimally combined to synthesize, within certain limits, the response of a detector with an arbitrary responsivity. However, it is known that the presence of noise in the photocurrent can degrade the performance of this algorithm significantly, depending on the choice of the responsivity spectrum to be synthesized. We generalize this algorithm to accommodate noise. The results are applied to quantum-dot mid-infrared detectors with bias-dependent spectral responses. Simulation and experiment are used to show the ability of the algorithm to reduce the adverse effect of noise on its spectral-tuning capability.

OCIS codes: 040.0040, 040.3060, 040.5570, 020.6580, 160.6000, 280.0280.

1. Introduction

Modern hyperspectral sensor systems, such as the Airborne Visible/Infrared Imaging Spectrometer (AVIRIS) or Hyperspectral Digital Imaging Collection Experiment (HYDICE), are capable of sensing the spectrum of a source in upwards of 200 bands of width 10–20 nm.[1–3] These systems are sophisticated and costly; they either use a dispersive optic element to spread the spectral content for each pixel to multiple line arrays[3] or use interferometric techniques that involve computation of the interference pattern and Fourier transform to obtain the spectral content.[4–8] In these systems, the spectrum or the interferogram corresponding to each pixel is captured on a single column of the array, leaving only one dimension of the array for gathering the spatial information. Multispectral systems, such as the Multispectral Thermal Imager,[9] are different from hyperspectral systems in that they use much fewer but wider bands, which results in reduced spectral resolution. However, multispectral sensing systems are simpler and easier to realize than hyperspectral sensing systems, as they require far less sophisticated optical front ends.

A key characteristic common to existing hyperspectral and multispectral sensors is that they cannot offer spectral resolutions below the resolution of their bands, which is a consequence of the spectrally nonoverlapping nature of the bands. On the other hand, multispectral detectors often have much wider responsivities than the desired resolution. Nonetheless, one can extract higher spectral resolution information from multiple detectors provided that the detectors exhibit spectrally overlapping responsivities.[10] Indeed, the use of spectral overlap in detectors to extract higher spectral resolution information is seen in nature. For example, the human eye uses overlapping spectral bands of three (in some cases four) different kinds of cone cells to sense color. Also, it has been shown that the use of overlapping spectral filtering in technology can improve performance of spectral sensing systems.[11]

An example of a class of detectors that can be utilized to produce spectrally overlapping bands is a subclass of the quantum-dot infrared photodetector (QDIP).[12–15] A QDIP may display a bias-dependent spectral responsivity due to the quantum-confined Stark effect, which is caused by an asymmetric potential profile. As the operating bias is varied, the responsivity changes by exhibiting a shift in its peak and, to a lesser extent, a variation in its shape. For this type of QDIP, a single detector can be operated at multiple biases sequentially, whereby the detector's

Ü. Sakoğlu (sakoglu@ece.unm.edu), M. M. Hayat, and J. S. Tyo are with the Department of Electrical and Computer Engineering, University of New Mexico, Albuquerque, New Mexico 87131. P. Dowd, S. Annamalai, K. T. Posani, and S. Krishna are with the Center for High Technology Materials and Department of Electrical and Computer Engineering, University of New Mexico, Albuquerque, New Mexico 87131.

Received 13 January 2006; revised 17 May 2006; accepted 17 May 2006; posted 17 May 2006 (Doc. ID 67214).

0003-6935/06/287224-11$15.00/0

responsivity changes each time the bias is varied. Therefore, a single QDIP can be exploited as different detectors.

Recently, Sakoglu *et al.*[10] reported a postprocessing algorithm that exploits the spectral overlap in multiple detectors in QDIPs to perform spectral sensing in the range of 3–8 μm with a resolution down to 0.50 μm, which is one fourth of the spectral resolution of the detector. It has also been shown theoretically that this technique is capable of performing some level of multispectral sensing.[10,16] The idea of the algorithm can be described as follows. Suppose that we operate the detector at K different biases and assume that for the kth bias the detector responsivity is $R_k(\lambda)$ (A/W). Now suppose that we are interested in combining the outputs of the detectors at various biases so as to mimic the response of a desired spectral filter, or band, which we denote by $r_c(\lambda)$. The first step of the algorithm is to form a weighted superposition of K responsivities to optimally approximate the multispectral band represented by $r_c(\lambda)$ (in the minimum mean-square sense). Then, by exploiting the linearity of the detector, these very weights can be used to form a weighted sum of the individual photocurrents from the detector, one for each operating bias. The resulting superposition would yield the best approximation of the output of the sought-after band represented by $r_c(\lambda)$. Synthesized responsivities obtained in this fashion can be continuously varied, within certain limits, in shape (unimodal or multimodal), width (narrowband or wideband), and location, depending on the requirements of each application. In other words, continuous spectral tuning is obtained.[10]

On the basis of the spectral overlap and diversity of QDIPs, approaches that use principal components analysis and canonical correlation analysis have been developed to study the performance of sensing.[17–22] The detectors' responsivities, which are functions of wavelength, are transformed into an uncorrelated function space. Since the spectra are practically sampled in wavelength, they have viewed sensing as an inner product between the sampled scene spectrum vector and the detector responsivity vector. They have transformed the vectors into an uncorrelated vector space in which the detectors' responsivities are decorrelated, and only the principal contributers are chosen to be used in sensing. Then, inner product outputs for each transformed detector constitute a new space. They have shown that sensing in this new space can give comparable results with a reduced data set. The new responsivities in the transformed space can still be overlapping in wavelength. In this work, however, instead of projecting the detectors' responsivities onto an uncorrelated space, we are interested in projecting them onto a new responsivity space that has certain properties: It is desired that the new responsivity functions have a certain center wavelength and certain resolution, as well as a certain shape. These properties might be wanted for certain applications in which the spectral information from certain bands is desired.

From a practical standpoint, however, the success of the aforementioned postprocessing-based tunable sensing strategy depends upon the level of noise in the measured current, which is attributable to dark current and the associated generation–recombination (shot) noise.[23–25] Since the algorithm is based on forming a weighted sum of photocurrents (usually with positive and negative signs), the noise variances corresponding to each weighted photocurrent accumulate, resulting in approximation error and poor signal-to-noise ratio (SNR).[16] Moreover, the effect of noise on the performance is shown to vary with the spectral width of the desired responsivity. In particular, as the full width at half-maximum (FWHM) of the desired responsivity decreases, the degradation due to noise effect becomes more severe. Intuitively, this is because the magnitudes of the weights needed to approximate a narrow responsivity become large and the noise accumulation becomes more pronounced; more specifically, the ratio of the sum of weights to the sum of their absolute values approachs zero. Therefore, there is a fundamental trade-off between the spectral resolution sought by the spectral-tuning algorithm and the noise-induced error.

In this paper we derive a generalization of the spectral-tuning algorithm[10,16] reported earlier to accommodate noise in the photocurrent. More generally, this work provides a framework for using a collection of sensors that have overlapping bands and different noise characteristics to synthesize outputs corresponding to a desired arbitrary band. The theory is applied to mid-infrared QDIPs fabricated by our group.

2. Theory

A. Photocurrent Model

The total current produced by a detector (labeled by k) can generally be written as

$$Y_k = y_{p,k} + d_k + N_k, \tag{1}$$

where N_k is the total noise (comprising one or more of the following components depending on the operating conditions: generation–recombination noise, signal-induced shot noise, Johnson noise, $1/f$ noise, etc.), d_k is the dark current representing the dc component of the current in the absence of illumination, and $y_{p,k}$ is the true photocurrent resulting from illumination. Both the dark current and the noise statistics are dependent upon temperature, the type of detector, as well as the operating bias of the detector. However, the noise components are assumed to be statistically independent from detector to detector. We denote the mean and variance of the noise by $\mu_{N,k}$ and $\sigma_{N,k}^2$ respectively. Moreover, we define the measurement SNR as the ratio of the photocurrent to the standard deviation of the noise,

$$\mathrm{SNR}_k \triangleq \frac{y_{p,k}}{\sigma_{N,k}}. \tag{2}$$

For a linear detector, the relationship among the detector's spectral response, the source spectrum, and the photocurrent can be cast as

$$y_{p,k} = A_e \int_{\lambda_{\min}}^{\lambda_{\max}} R_k(\lambda) g(\lambda, Z) \mathrm{d}\lambda, \tag{3}$$

where $g(\lambda, Z)$ (W cm^{-2} μm^{-1}) is the spectral irradiance of the source (combined with any other filters and/or effects in the scene) at temperature Z (kelvin) and A_e is the effective source-to-detector area that combines all the coupling factors. For simplicity we assume that A_e does not vary from detector to detector. For the sake of the analysis to follow, it would be convenient to embed the noise into the integral above and obtain an equivalent expression for the noisy photocurrent. By using Eqs. (2) and (3), we can write

$$\begin{aligned} Y_{p,k} &\triangleq y_{p,k} + N_k \\ &= A_e \int_{\lambda_{\min}}^{\lambda_{\max}} \left[R_k(\lambda) + \frac{N_k}{A_e \int_{\lambda_{\min}}^{\lambda_{\max}} g(\lambda', Z) \mathrm{d}\lambda'} \right] g(\lambda, Z) \mathrm{d}\lambda, \end{aligned} \tag{4}$$

$$\begin{aligned} &\approx A_e \int_{\lambda_{\min}}^{\lambda_{\max}} \left[R_k(\lambda) + \frac{R_k(\lambda) N_k}{A_e \int_{\lambda_{\min}}^{\lambda_{\max}} R_k(\lambda') g(\lambda', Z) \mathrm{d}\lambda'} \right] \\ &\quad \times g(\lambda, Z) \mathrm{d}\lambda, \end{aligned} \tag{5}$$

$$= A_e \int_{\lambda_{\min}}^{\lambda_{\max}} R_k(\lambda) \left(1 + \frac{N_k}{\sigma_{N,k} \mathrm{SNR}_k} \right) g(\lambda, Z) \mathrm{d}\lambda. \tag{6}$$

In Eq. (6), we can identify the noisy responsivity as

$$\tilde{R}_k(\lambda) \triangleq R_k(\lambda) \left(1 + \frac{N_k}{\sigma_{N,k} \mathrm{SNR}_k} \right). \tag{7}$$

We introduce the approximation in Eq. (5) to get rid of the dependence on source irradiance, $g(\lambda, Z)$, i.e., to make the algorithm source independent, since the goal of the algorithm is to sense the source irradiance. This approximation turns into an equality when the variation in $R_k(\lambda)$ is negligible over the integration range. However, in that case it would not serve our algorithm since there would not be any spectral diversity.

The above approximation can be equivalently restated as $R_k(\lambda) \int_{\lambda_{\min}}^{\lambda_{\max}} g(\lambda') \mathrm{d}\lambda' \approx \int_{\lambda_{\min}}^{\lambda_{\max}} R_k(\lambda') g(\lambda') \mathrm{d}\lambda'$. From the first mean value theorem for integration, we know that at least one λ satisfies equality in the approximation. The theorem states that if $R(\lambda') : [\lambda_{\min}, \lambda_{\max}] \to \mathbb{R}$ is continuous and $g(\lambda') : [\lambda_{\min}, \lambda_{\max}] \to \mathbb{R}$ is a integrable positive function, then there exists a number λ in $(\lambda_{\min}, \lambda_{\max})$ such that $\int_{\lambda_{\min}}^{\lambda_{\max}} R_k(\lambda') g(\lambda') \mathrm{d}\lambda' = R_k(\lambda') \int_{\lambda_{\min}}^{\lambda_{\max}} g(\lambda') \mathrm{d}\lambda'$. Moreover, since the detectors' responses are close to 0 near $\lambda_{\min}$ and $\lambda_{\max}$, and have peak(s) in between, there exist at least two λ values for which the equality holds since this condition leads to the existance of a set of $\lambda = \{\lambda_1, \lambda_2, \ldots\}$ such that $\{R_k(\lambda_1) = R_k(\lambda_2) = \ldots\}$. Furthermore, due to nature of our spectral-tuning algorithm, which combines (with positive and negative weights) the detectors' spectral response, the associated approximation error also gets averaged. Thus, when we compare the spectral-tuning results of the original and the noise-modified algorithm, we see that this approximation does not seem to affect the noise-modified algorithm so badly as to make it worse, as we present in Section 3.

B. Algorithm Development

As described in Section 1, the goal of the algorithm is to synthesize the photocurrent response of an arbitrary desired responsivity, $r_c(\lambda)$ associated with center wavelength λ_c, by utilizing the outputs of multiple detectors with spectrally overlapping responsivities. The shape and width of $r_c(\lambda)$ and the location of the filter centers, λ_c ($c = 1, \ldots, C$), all depend on the application. Let us assume that we have a collection of K detectors, $\mathcal{D} = \{D_1, \ldots, D_K\}$, each having spectral responsivity $R_k(\lambda)$, $k = 1, \ldots, K$. By combining the detector-dependent responsivities $R_k(\lambda)$, the desired responsivity $r_c(\lambda)$ can be approximated linearly as

$$\hat{r}_c(\lambda) = \sum_{k=1}^{K} w_{c,k} \tilde{R}_k(\lambda). \tag{8}$$

Our goal is to find the set of weights, $\mathbf{w}_c \triangleq [w_{c,1}, \ldots, w_{c,K}]^T$, so that we can best approximate the ideal response

$$y_c = A_e \int_{\lambda_{\min}}^{\lambda_{\max}} g(\lambda, Z) r_c(\lambda) \mathrm{d}\lambda \tag{9}$$

by means of the synthesized response $\hat{Y}_c = \sum_{k=1}^{K} w_{k,c} Y_{p,k}$. It has been shown[10] that in the absence of noise, the best approximate response $\hat{Y}_c$, in the minimum mean-square error sense, is equivalent to the response of the detector whose spectral response is $\hat{r}_c(\lambda) = \sum_{k=1}^{K} w_{c,k} \tilde{R}_k(\lambda)$ that best approximates the desired $r_c(\lambda)$, in which case

$$\hat{Y}_c = A_e \int_{\lambda_{\min}}^{\lambda_{\max}} g(\lambda, Z) \left[\sum_{k=1}^{K} w_{c,k} \tilde{R}_k(\lambda) \right] \mathrm{d}\lambda. \tag{10}$$

We now incorporate noise into the algorithm by seeking the vector $\mathbf{w}_c$ that minimizes the average of the mean-square error $\epsilon^2(r_c, \mathcal{D}) \triangleq \mathsf{E}\left[\left| y_c - \hat{Y}_c \right|^2 \right]$, where E denotes ensemble averaging. By substituting Eqs. (9) and (10) in this definition, we obtain

$$\epsilon^2(r_c,\ \mathcal{D}) = \mathsf{E}\left\{ \left| A_e \int_{\lambda_{\min}}^{\lambda_{\max}} g(\lambda,\ Z)\left[r_c(\lambda) - \sum_{k=1}^{K} w_{c,k} R_k(\lambda) \times \left(1 + \frac{N_k}{\sigma_{N,k}\mathrm{SNR}_k}\right)\right] \mathrm{d}\lambda \right|^2 \right\}. \quad (11)$$

To remove the dependence of the error expression on the spectral irradiance $g(\lambda)$, we compute an upper bound to this expression using the Schwarz inequality.[26] We assume that the noise N_k has zero mean for all detectors and that noise for different detectors is independent. We then discretize the integral and convert Eq. (11) into matrix form (see Appendix A for a detailed derivation) and obtain the expression to be minimized as

$$\frac{\Delta\lambda}{L} \sum_{j=1}^{L} \left\{ r_c^{\,2}(\lambda_j) - 2 r_c(\lambda_j)\left[\sum_{k=1}^{K} w_{c,k} R_k(\lambda_j)\right] + \left[\sum_{k=1}^{K} w_{c,k} R_k(\lambda_j)\right]^2 + \left[\sum_{k=1}^{K} w_{c,k}^{\,2} \frac{R_k^{\,2}(\lambda_j)}{\mathrm{SNR}_k^{\,2}}\right]\right\}. \quad (12)$$

In the above, L is the number of wavelength locations at which the spectrum was sampled, $\lambda_1 = \lambda_{\min}$, $\lambda_L = \lambda_{\max}$, and $\Delta\lambda = \lambda_{\max} - \lambda_{\min}$. Defining the vector forms of the discretized spectrum as $\mathbf{R}_k \triangleq [R_k(\lambda_1), \ldots, R_k(\lambda_L)]^T$ and $\mathbf{r}_c \triangleq [r_c(\lambda_1), \ldots, r_c(\lambda_L)]^T$, and the matrix of spectral response $\mathbf{A} \triangleq [\mathbf{R}_1, \ldots, \mathbf{R}_K]$, the weight vector that minimizes the discretized mean-square error is found to be (see Appendix A for derivation)

$$\mathbf{w}_c = \left[\mathbf{A}^T\mathbf{A} + \mathbf{\Phi}\right]^{-1}\mathbf{\Pi}_c, \quad (13)$$

where

$$\mathbf{\Phi} = \begin{bmatrix} \dfrac{\mathbf{R}_1^{\,T}\mathbf{R}_1}{\mathrm{SNR}_1^{\,2}} & 0 & \cdots & 0 \\ 0 & \dfrac{\mathbf{R}_2^{\,T}\mathbf{R}_2}{\mathrm{SNR}_2^{\,2}} & \cdots & 0 \\ \vdots & \vdots & \ddots & \vdots \\ 0 & 0 & \cdots & \dfrac{\mathbf{R}_K^{\,T}\mathbf{R}_K}{\mathrm{SNR}_K^{\,2}} \end{bmatrix}, \quad (14)$$

$$\mathbf{\Pi}_c = \mathbf{A}^T\mathbf{r}_c. \quad (15)$$

It can be seen from expression (12) that in the absence of noise, the minimization problem reduces to the minimization of the error in the approximation of the filter $r_c(\lambda)$ (or equivalently $\mathbf{r}_c$). However, such minimization can produce a solution that is highly fluctuating as a function of λ; therefore, it is desirable to include a regularization term that penalizes nonsmoothness in the approximation.[10] As such, we include a regularization term, $\alpha\|\mathbf{Q}\mathbf{A}\mathbf{w}_c\|^2$, in the mean-square error, so that the regularized version of

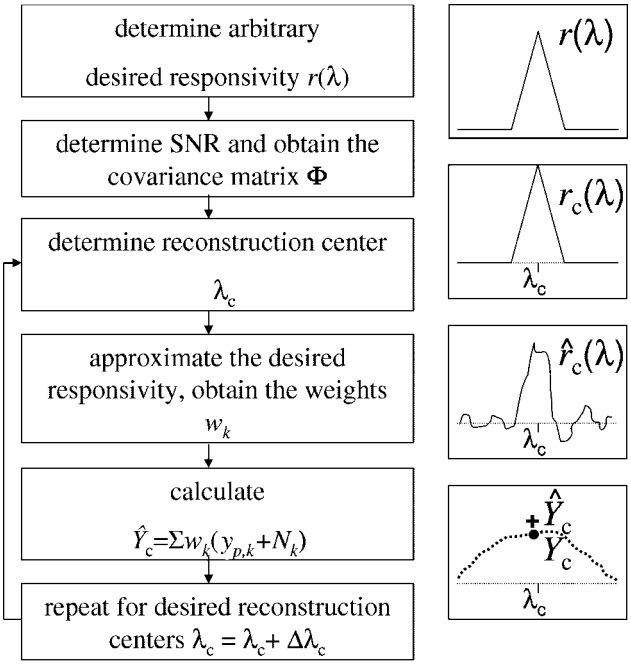

Fig. 1. Flow chart of the entire noise-modified spectral-tuning algorithm.

expression (12) becomes

$$\Delta\lambda L^{-1}\left[\|\mathbf{r}_c - \mathbf{A}\mathbf{w}_c\|^2 + \mathbf{w}_c^{\,T}\Phi\mathbf{w}_c + \alpha\|\mathbf{Q}\mathbf{A}\mathbf{w}_c\|^2\right], \quad (16)$$

where $\mathbf{Q}$ is a regularization matrix (typically a high-pass filter). As in our earlier work, we take

$$\mathbf{Q} = \begin{bmatrix} 1 & -1 & & & & & \\ -1 & 2 & -1 & & & & \\ & & \ddots & & & & \\ & & & -1 & 2 & -1 & \\ & & & & -1 & 1 & \end{bmatrix}, \quad (17)$$

which is the Laplacian operator, and α is the corresponding weight for the penalization term and can be adjusted according to the desired level of roughness penalization.[10] (In our applications, $\alpha = 0.04$ gave good results.) We finally obtain an expression for the weights that minimize expression (16):

$$\mathbf{w}_c = \left[\mathbf{A}^T\mathbf{A} + \mathbf{\Phi} + \alpha\mathbf{Q}^T\mathbf{A}^T\mathbf{A}\mathbf{Q}\right]^{-1}\mathbf{\Pi}_c. \quad (18)$$

A flow chart summarizing the entire algorithm is shown in Fig. 1.

3. Application to Quantum-dot Infrared Detectors

In this section we apply the noise-modified spectral-tuning algorithm developed in Subsection 2.B to QDIPs that have been recently fabricated and characterized at the Center for High Technology Materials at the University of New Mexico. The QDIP device used in our application has an asymmetric dots-in-a-well (DWELL) structure, sandwiched between highly

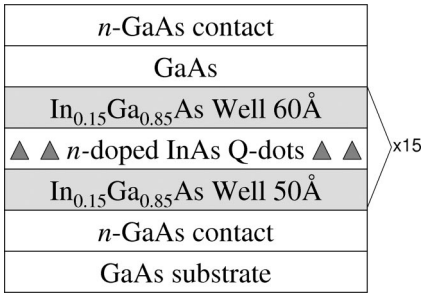

Fig. 2. Schematic of the 15-layer asymmetric InAs/$In_{0.15}Ga_{0.85}As$ DWELL detector structure sandwiched between two highly doped *n*-GaAs contact layers, grown on a semi-insulating GaAs substrate.[27]

n-doped GaAs layers and grown on a semi-insulating GaAs substrate. A simple schematic of the device is shown in Fig. 2. The active region of the detector consists of 15 layers of InAs quantum dots in an $In_{0.15}Ga_{0.85}As$ well.[27] The well is asymmetric in the sense that the width of the top and bottom well layers are different (60 and 50 Å), which leads to photoresponsivities that can be spectrally tuned by changing the applied bias voltage. The width of the quantum-dot layer is only 5–8 Å, and the total thickness of the detector is ~3.5 μm. Devices with different diameter apertures, ranging from 25 to 300 μm, were fabricated on a 6-by-6 array. Data from a 300 μm diameter aperture detector were chosen for our application. This was done due to the large aperture area, which yields a large photocurrent.

A. Experiment and Measurement Process

The spectral response of the QDIP was measured at a temperature of 50 K by using a Fourier-transform infrared spectrometer and was averaged over 64 measurements for each bias voltage, $[V_1, \ldots, V_{17}] = [4, 3.75, \ldots, 2, -1.75, -2.25, \ldots, -3.5]$ V. The set of responses was obtained in a wavenumber domain ranging from 500 to 5000 cm^{-1}, corresponding to 2–20 μm. The responses were resampled to fit in a linear wavelength grid, with 0.01 μm intervals in the range of 2.51–11.00 μm. The parameters L and $\Delta\lambda$, used in the algorithm, are therefore 850 and 8.5 μm, respectively. The spectral response was also normalized so that the peak value is equal to unity, and the resulting peak-normalized spectral responses, denoted by $f_k(\lambda)$, were obtained. The average total current y_k and average dark current d_k of the detector for the same set of voltages were also measured. The average photocurrents $y_{p,k}$ were then computed by taking the difference between the measured total current and the dark current, under unfiltered blackbody source illumination. In total, 30 and 110 measurements were used for the average total and dark-current response, respectively. The standard deviation of the current noise $\sigma_{N,k}$ was also estimated empirically from the dark-current measurements.

Next, the bias-dependent peak responsivity R_k^p of the device was calculated by using the relation[28,29]

$$y_{p,k} = A_e \int_{\lambda_{\min}}^{\lambda_{\max}} R_k^p f_k(\lambda) g(\lambda, Z) \mathrm{d}\lambda. \tag{19}$$

In our devices, the effective source-to-detector area was found to be $A_e = 10^{-6}$ cm^2. The responsivity of the detector can now be obtained by multiplying the peak responsivity with the peak-normalized spectral response

$$R_k(\lambda) = R_k^p f_k(\lambda). \tag{20}$$

We define the transmittance of the source-to-detector optical system, or the relative spectrum (with respect to a blackbody source), as

$$G(\lambda, Z) = \frac{g(\lambda, Z)}{W(\lambda, Z)}, \tag{21}$$

where $W(\lambda, Z) = [2\pi hc^2/\lambda^5]/[\exp(hc/\lambda k_B Z) - 1]$ (W cm^{-2} μm^{-1}) is the blackbody spectral density determined by Planck's law at the source temperature Z (h is Planck's constant, k_B is the Boltzmann constant, and c is the speed of light). One can pick either $g(\lambda)$, the total irradiance, or $G(\lambda)$, the transmittance, as the spectrum to be reconstructed, since one can be calculated from the other (as long as the source temperature is known). In our application, we consider two cases: (1) placing no filter in front of the detector so that $G(\lambda) \equiv 1$, or equivalently $g(\lambda, Z)$ is the blackbody irradiance at the temperature Z; and (2) placing a 3 mm polystyrene filter in front of the detector so that $G(\lambda)$ is the transmittance of the filter. In our experiment, the blackbody source incident on the detector was at room temperature (300 K).

The bias-dependent total current profile, y_k, $k = 1, \ldots, K = 17$, with and without the 3 mm polystyrene filter in the view of the detector and the dark-current profile, d_k, and its standard deviation are all shown in Fig. 3. These were measured at the detector temperature of 50 K. The peak-normalized spectral responses of the device, $f_k(\lambda)$, measured at the same temperature for the prescribed set of bias voltages, are shown in Fig. 4. It can be seen in Fig. 4 that, as the bias voltage is varied, the shape of the spectral response changes, by means of the change in the height of dominant and secondary peaks. Also note that the FWHM of the main peaks of the response change from 1.5 μm (at 4 V) to 2 μm (at −2 V). The narrower the FWHM of the responsivities, the better the algorithm can approximate narrower responsivities $\mathbf{r}_c$.

For the devices considered, much of the range of the spectral tuning lays in the atmospheric absorbtion region; however, we will ignore this limitation in this paper since our focus is to prove the concept of algorithmic spectral tuning. We have recently demonstrated QDIPs with peaks of the bias-dependent spectral responses spanning the range 8–12 μm.

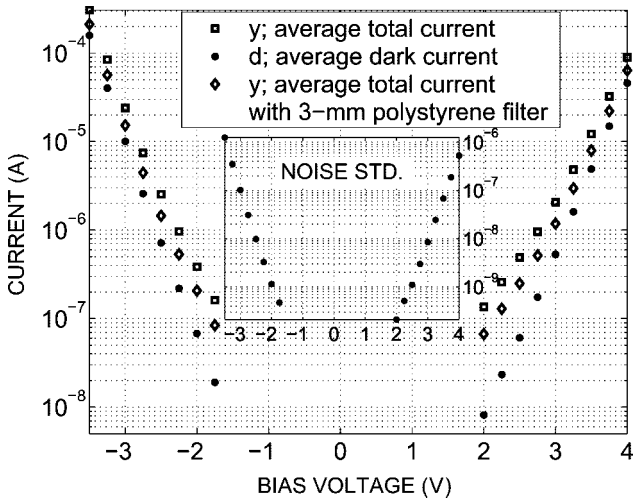

Fig. 3. Total and dark-current profiles of the DWELL detector with a 300 μm diameter at 50 K. The open diamonds and open squares represent the total current with and without the 3 mm polystyrene filter, respectively. The filled circles represent the dark current at 50 K. Inset: Noise standard deviation.

B. Experiments with Simulated Noise

To demonstrate the effect of noisy data on the old version of the algorithm[10] (which does not account for the noise), we calculated the weights $\mathbf{w}_c$ according to Eq. (13) with the noise variances $\sigma_{N,k}{}^2$, or equivalently $1/\mathrm{SNR}_k{}^2$, set to zero in Eq. (14). We then simply added noise (Poisson-distributed random variables[24] with specified variances) to the photocurrents before using them in the weighted superposition. On the other hand, to demonstrate the effectiveness of the noise-modified algorithm in mitigating noise, we used Eq. (13), with the actual noise parameters, to arrive at the noise-modified weights. The average value of the SNR, as defined in Eq. (2) and taken over the 17 bias voltages, was calculated for the two sources used; these SNRs are 226 for the unfiltered blackbody source and 163 for the 3 mm polystyrene-filtered blackbody source. These values correspond to our dark-current measurements at a detector temperature of 50 K. The difference in the SNR, which is due to the change in the signal (as the filter was introduced), was compensated by a multiplicative factor of 0.72 to obtain the same level of SNR for both cases.

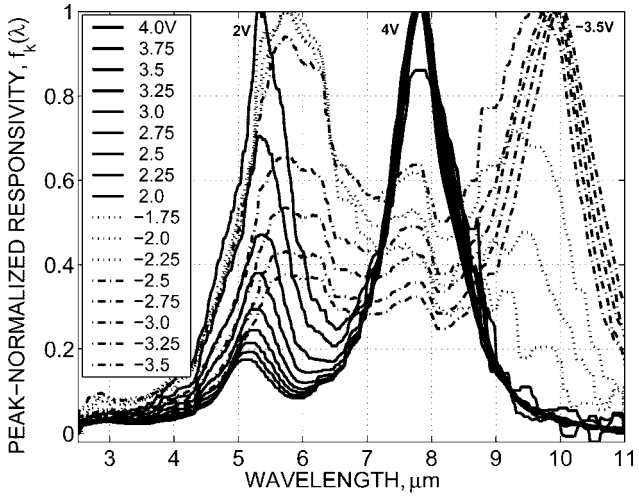

Fig. 4. Peak-normalized spectral response of the QDIP for different bias voltages.

1. *Trade-off between Spectral Resolution and Approximation Error*

We applied the algorithm to obtain spectral tuning and consequently the reconstruction of the spectra of the two different sources. In each case, we performed spectral reconstruction of the sources from the photocurrents by repeatedly applying the algorithm, with a triangular tuning responsivity and a specified desired FWHM, while varying the center wavelengths of the triangular responsivity from the collection {5.0, 4.2, . . . , 9.8, 10.0 μm}. The spectral reconstruction was repeated for different SNRs, ranging from 0.02 (low) to 20,000 (high), and for different desired FWHMs of the triangular responsivity in the range from 0.5 μm (narrow) to 2.5 μm (wide).

Representative spectral reconstructions are shown in Fig. 5 for a narrow triangular responsivity with a FWHM of 0.5 μm and in Fig. 6 for a wide desired responsivity of 1.5 μm. Included in these figures are (i) the true spectral irradiance viewed by the detector normalized by the blackbody spectrum (solid curve); (ii) spectral reconstruction of the normalized source spectrum, using ideal triangular filters of the desired FWHM, shown as filled circles and used as a benchmark for the performance as there is no error in approximating the tuning filters; (iii) spectral reconstruction of the normalized source spectrum using the old spectral-tuning algorithm, shown as crosses; and (iv) spectral reconstruction of the normalized spectrum using the new noise-modified spectral-tuning algorithm, shown as plusses. The average SNR used to generate Fig. 5 is 100. For this level of SNR, we see that the old algorithm is affected severely by the presence of noise in the data, while the new algorithm performs reasonably well despite the noise. Spectral reconstructions with higher SNRs (>2000) were also obtained (results not shown); in this case, both old and noise-modified algorithms perform well yielding a reconstruction that is very close to the ideal reconstruction. High SNR levels are achievable at very low detector temperatures, or with other noise-reduction techniques such as time averaging of the photocurrent, which we discuss in Subsection 3.B.2.

The results in Fig. 6 show a slightly reduced overall error in the spectral reconstruction at the expense of degradation in spectral resolution. Intuitively, achieving a high spectral resolution requires the algorithm to generate weights with large magnitudes, possibly with varying signs, as the algorithm attempts to meet the challenge of approximating a narrow filter using the relatively broad bias-dependent responsivities of the QDIP. This, in turn, results in accentuated noise accumulation as the magnitudes of

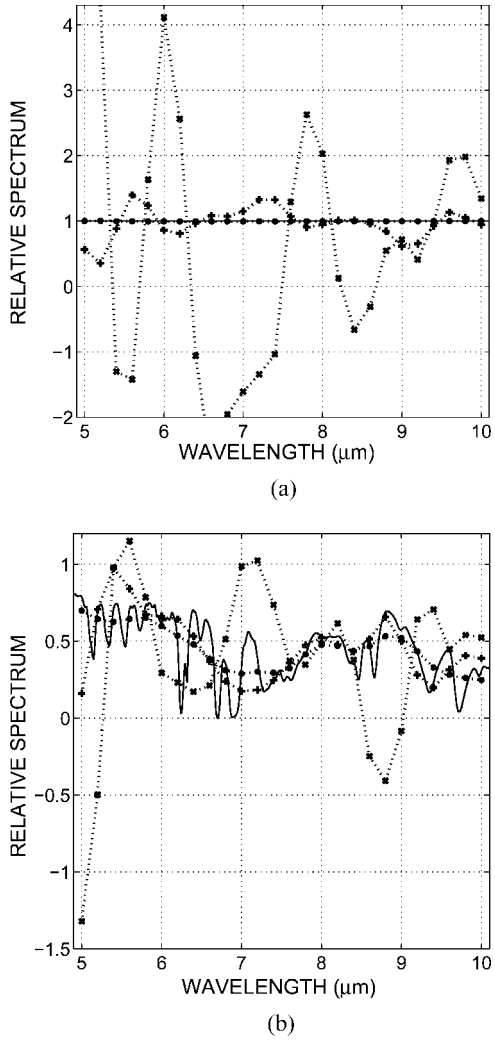

Fig. 5. Performance of the algorithm in synthesizing the relative power spectrum of (a) a blackbody source and (b) a 3 mm polystyrene filter by using the desired responsivity of ideal triangular filters of FWHM of 0.5 μm, under moderately low noise (with a SNR of 100). The crosses and plusses represent the original tuning algorithm that does not accommodate the noise and the new noise-modified tuning algorithm, respectively. The filled circles represent the reconstruction by using ideal responsivity. Under very low noise (for a SNR of more than ~2000), the ideal reconstruction (filled circles) and algorithms' reconstruction (plusses and crosses) overlap.

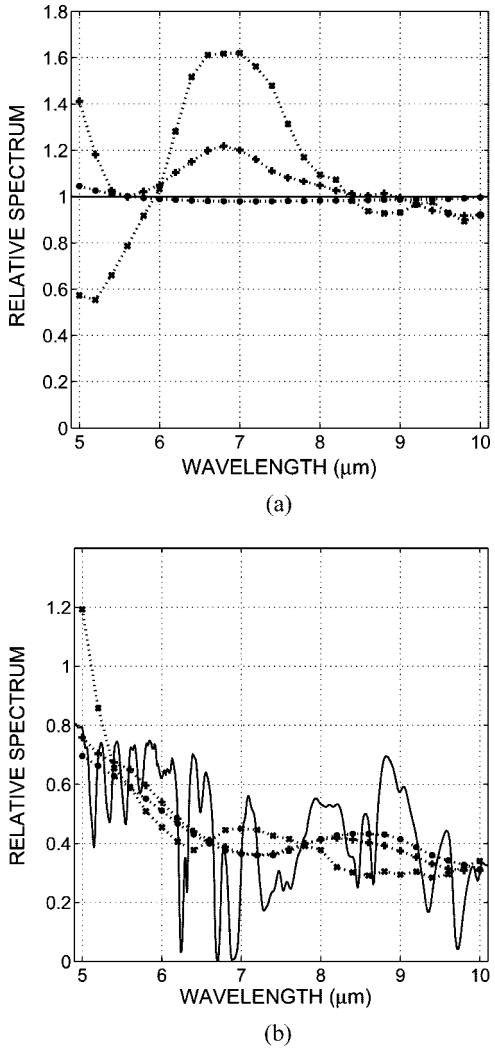

Fig. 6. Same as Fig. 5 but with a wider desired triangular responsivity with a FWHM of 1.5 μm.

the weights increase. Thus, there is a fundamental trade-off between synthesized spectral resolution and robustness to noise. Indeed, calculations confirm that there is a strong trend of increase in the sum of absolute values of the weights (over all bias voltages) as the desired FWHM is decreased. For example, in the case of the old algorithm with a triangular filter centered at $\lambda_c = 6.0$ μm, the sum of absolute values of the weights takes the values of 55,751, 62,666, and 246,340 for FWHM values of 2.5, 1.5, and 0.5 μm, respectively, which directly translates to an increase in noise accumulation in the weighted superposition as the FWHM is reduced. In contrast, the noise-modified algorithm shows a similar trend in the magnitudes of the weights only at high photocurrent SNRs (>200), but the trend weakens and eventually disappears as the SNR decreases. For example, for an SNR value of 0.2, the noise-modified algorithm renders the values of 4604, 4897, and 4763, for the sum of the absolute values of the weights, for FWHM values of 2.5, 1.5, and 0.5 μm, respectively. The decrease in the weights' magnitudes in the noise-modified algorithm is a direct consequence of the algorithm's attempt to combat noise. The sample standard deviation of the weights, which is another measure of the magnitude of the weights, also shows a similar trend as the sum of absolute values of the weights (results not shown).

2. *Role of Photocurrent Signal-to-Noise Ratio*

For each SNR level, the tuning algorithm was applied 1000 times, with the noise in the photocurrent varying randomly from trial to trial. The errors of the spectral reconstruction, normalized with respect to the true value of the target spectrum, were then calculated and averaged over the 1000 trials and over the construction

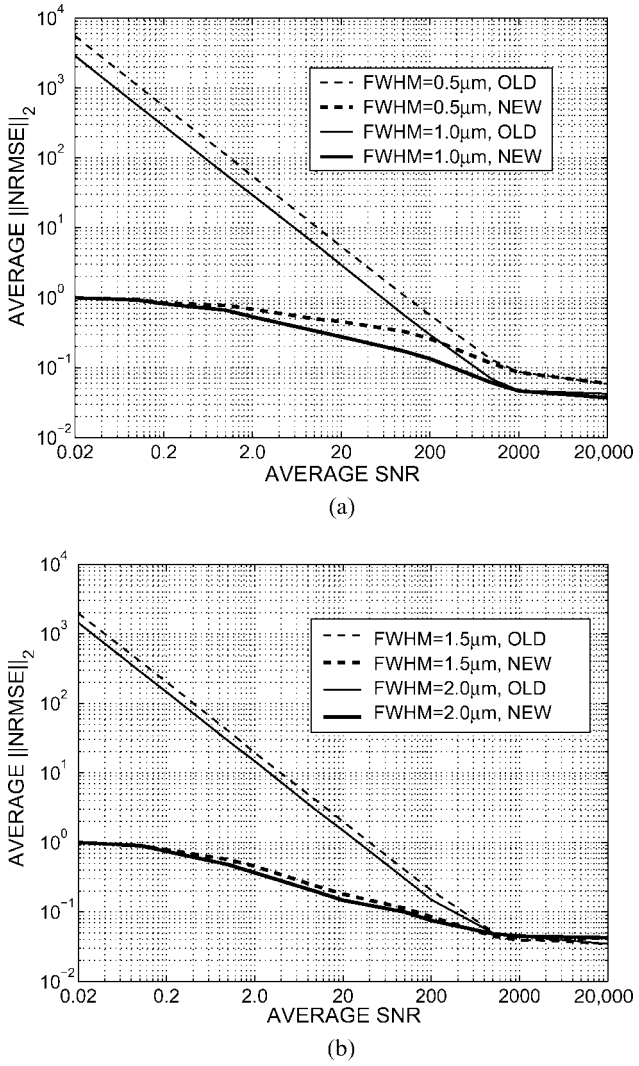

Fig. 7. Comparison of the original algorithm that does not accommodate noise (thin curves) and the noise-modified algorithm (thick curves); the performance shown in terms of average normalized root-mean-square error (NRMSE) versus the photocurrent SNR for desired resolution of (a) narrow FWHM of 0.5 μm (dashed curves) and 1.0 μm (solid curves) and (b) wide FWHMs of 1.5 μm (dashed curves) and 2.0 μm (solid curves).

wavelengths. We then took the square root of this empirical error to obtain the average normalized root-mean-square error (NRMSE). This gives an average normalized error for each SNR for a given FWHM of the triangular responsivity, as shown in Figs. 7(a) and 7(b). In these figures, we present results for the case of reconstructing the blackbody spectrum for (a) narrow (FWHM = 0.5 and 1.0 μm) and (b) wide (FWHM = 1.5 and 2.0 μm) desired spectral resolutions. The performance of the algorithm was studied for both the old (thin curves) as well as the noise-modified algorithm (thick curves). Note that the maximum value of the NRMSE is 1 (i.e., 100%) for the noise-modified algorithm, since the weights approach zero as the noise power increases.

We observe that the average NRMSE is significantly less for the noise-modified algorithm than that for the old algorithm. For example, for an average SNR level of 2, the NRMSE is reduced by 18 dB. In particular, the results shown in Fig. 7 demonstrate that the noise-modified algorithm requires much less photocurrent SNR than the original algorithm. For example, for the case when the FWHM is 1.0 μm, the noise-modified algorithm can attain an average error of 20%, for an average SNR level of 63, while the old algorithm will require an average SNR level of 316 (an increase of five in SNR) to achieve the same performance. For the case when the FWHM is 1.5 μm, the required average SNR levels for the same error level are 210 and 16, respectively, for the old and the noise-modified algorithms.

We also observe in Figs. 7 that the average NRMSE in the reconstruction decreases as the FWHM is increased, signifying the trade-off, as described earlier, between spectral resolution and robustness to noise. For a fixed operating temperature, the SNR can be increased by either increasing the integration time of the detector or by repeating the reconstruction and averaging the results. Note that averaging the results over M photocurrent samples increases the SNR effectively by a factor of $M^{1/2}$. However, such averaging will slow the speed of the reconstruction. The noise-modified algorithm, albeit, will help reduce this speed overhead by a factor ranging from 25 to 175 for the devices considered, depending on the desired accuracy.

Table 1. Five-band Multispectral Performance of the Algorithm in Synthesizing the Relative Power Spectrum of a Blackbody Source and a 3 mm Polystyrene Filter in the Case of Moderate Noise (SNR = 20) Using a Synthesized Triangular Filter with FWHM = 1.0 μm

λ_c	Actual	Ideal	Old	New
Black-body Source				
5	1.0000	1.0180	−5.6348	1.3027
6	1.0000	0.9933	−1.9762	1.0701
7	1.0000	0.9901	12.654	0.8619
8	1.0000	0.9918	−0.2698	0.9624
9	1.0000	0.9943	−1.0783	0.8660
d_1	0	0.0238	13.9514	0.3674
d_0	1.0166	1.0054	14.2562	1.0073
d_{nor}	2	1.9075	0.0217	0.9311
3 mm Polystyrene Filter				
5	0.7905	0.6962	1.0854	0.7258
6	0.6210	0.5533	−0.6804	0.6115
7	0.3315	0.3224	2.0281	0.3962
8	0.5330	0.4249	0.1977	0.3902
9	0.5745	0.4480	0.4894	0.2898
d_1	0	0.2051	2.1861	0.3315
d_0	1.0166	1.1789	2.1892	1.2112
d_{nor}	2	1.4072	0.0013	1.1405

4. Potential for Multispectral-based Target Classification

We used the tuning algorithm to perform multispectral target discrimination based on 5-band sensing. Table 1 lists the details of the 5-band representation of the two source spectra considered (the blackbody

source with and without the polystyrene film) with the old and noise-modified spectral-tuning algorithms. Individual bands correspond to triangular filters with a FWHM of 1 μm, centered at various wavelengths. The SNR is assumed as 200. The first column of the table shows the centers of the five bands, ranging from 5 to 9 μm. The second column depicts the actual values of the target spectrum, sampled at the center wavelengths, while the third column is the ideal reconstruction using the triangular filters with a FWHM of 1 μm. The fourth and fifth columns are the reconstruction results using the old algorithm and the noise-modified algorithm. Separability between the two target spectra can be examined by comparing the Euclidean distance between the 5-band reconstruction (columns four or five in Table 1) and the actual samples of the spectra (column 2 in Table 1) in the five-dimensional multispectral feature space, comprising the reconstructed outputs of each band. More precisely, we have adopted a simple performance metric, defined by[30]

$$d_{\mathrm{nor}} = \frac{d_0 - d_1}{0.5(d_0 + d_1)}, \tag{22}$$

where d_1 is the distance between the reconstructed 5-band feature vector and the true spectrum samples, and d_0 is the distance between the reconstructed 5-band feature vector and the wrong spectrum. Note that the best separation is achieved when $d_{\mathrm{nor}} = 2$, which corresponds to $d_1 = 0$. On the other hand, the worst performance occurs when $d_{\mathrm{nor}} = 0$, which corresponds to the case when separation is impossible under this simple distance-based metric.

Table 1 corresponds to the cases for which the true hypothesis is the unfiltered blackbody source and the 3 mm polystyrene-filtered blackbody source. The results are for a noisy case in which the SNR = 20 (low SNR). We can see that the noise-modified algorithm results in much less distance to the true spectrum, and hence larger d_{nor}. For example, as shown in Table 1 for a blackbody source, the noise-modified algorithm yields $d_{\mathrm{nor}} = 0.9311$, which is much closer to that of the ideal reconstruction (for which $d_{\mathrm{nor}} = 1.9075$) than that of the old algorithm (for which $d_{\mathrm{nor}} = 0.0217$). These results show that under low SNR conditions, only the noise-modified algorithm can be used for successful target discrimination, and the separation offered by the noise-modified algorithm is quite close to an ideal multispectral sensor. When the noise power is small (e.g., when the SNR is greater than 2000), the reconstruction results for the old and new algorithm become comparable (results not shown here).

The error in the reconstructed spectra depends upon the reconstruction wavelength, which, in turn, is mainly governed by (1) the shapes of the basis detector spectra $R_k(\lambda)$, (2) the target spectrum $g(\lambda)$, and (3) the shape of the desired target responsivity $r_c(\lambda)$. Near the wavelength regions where the basis spectra have well-defined peaks, the reconstruction error decreases since the associated ideal filter approximation error is low. For example, if we consider the blackbody spectrum reconstruction results shown in Table 1 [also shown in Fig. 5(a)] to see the effect of the location of the peaks, we see that the error is least around 8 μm, where some of basis spectra corresponding to the bias range {4–2.5 V} have peaks according to Fig. 4. On the other hand, the error is worse around 5 and 7 μm where the basis spectra do not exhibit major peaks. From the polystyrene reconstruction in Table 1 [also shown in Figs. 5(b) and 6(b)], we observe how the accuracy of the reconstruction is also dictated by the shape of the source spectrum; fine features of the spectrum (narrow dips and peaks) cannot be reconstructed well due to the limited resolution of the basis spectra. From our experience, we observed that we cannot go below the target resolution of FWHM = 0.5 μm with the resolution of the basis spectra of the current QDIPs produced, which have a FWHM of approximately 2 μm. In addition to tuning in the 3–8 μm range reported earlier,[10] the device used in this paper allows us to tune in the range of 5–10 μm. We have recently developed a QDIP that would allow us to have tuning in the 8–12 μm range.

5. Conclusions

We have developed a spectral-tuning algorithm that is based on exploiting the presence of spectral overlap and spectral diversity in the responsivities of a collection of detectors to synthesize the output of a desired arbitrary band. This work is an important generalization of an earlier version of the algorithm to accommodate and compensate for noise in the output of the detectors. We have applied the algorithm to quantum-dot mid-infrared photodetectors (QDIPs) developed by our group, and have shown approximate, continuous spectral tuning for two different source spectra, namely, a blackbody source with and without a 3 mm polystyrene filter in the range of 5–10 μm. As a measure of performance, we used the normalized root-mean-square error as a function of different noise levels and desired tuning resolutions. We have shown that the SNR requirements for the noise-modified algorithm are significantly reduced when compared with the old algorithm, which did not accommodate photocurrent noise. This promises robustness to photocurrent noise with certain limitations depending on the spectral diversity in the detectors' responsivities. Also, as the desired spectral resolution of the tuning is reduced, the required SNR becomes less. Therefore, as the desired width of the tuning filter is increased, which is the case in many wideband applications, the algorithm becomes more robust to noise and the overall tuning error decreases. This shows a fundamental trade-off between the resolution of spectral tuning and robustness to noise.

Appendix A

The expectation of the square of the error between the actual and the approximated outputs can be writ-

ten as [see Eqs. (9), (10), and (11) in Section 2]

$$\mathsf{E}\left[\left|y_c-\hat{Y}_c\right|^2\right]=\mathsf{E}\left\{\left|A_e\int_{\lambda_{\min}}^{\lambda_{\max}} g(\lambda,\,Z)\left[r_c(\lambda)-\sum_{k=1}^{K} w_{c,k}R_k(\lambda)\left(1+\frac{N_k}{\mathrm{SNR}_k\sigma_{N,k}}\right)\right]\mathrm{d}\lambda\right|^2\right\}. \tag{A1}$$

After applying the Schwarz inequality,[26] we can write

$$\mathsf{E}\left[\left|y_c-\hat{Y}_c\right|^2\right]\le \mathsf{E}\left[A_e\int_{\lambda_{\min}}^{\lambda_{\max}}|g(\lambda,\,Z)|^2\mathrm{d}\lambda\right]\times\left[\int_{\lambda_{\min}}^{\lambda_{\max}}\left|r_c(\lambda)-\sum_{k=1}^{K} w_{c,k}R_k(\lambda)\left(1+\frac{N_k}{\mathrm{SNR}_k\sigma_{N,k}}\right)\mathrm{d}\lambda\right|^2\right]. \tag{A2}$$

Since the term in the first set of brackets is a constant, the minimization reduces to the minimization of

$$\mathsf{E}\left[\int_{\lambda_{\min}}^{\lambda_{\max}}\left|r_c(\lambda)-\sum_{k=1}^{K} w_{c,k}R_k(\lambda)\left(1+\frac{N_k}{\mathrm{SNR}_k\sigma_{N,k}}\right)\mathrm{d}\lambda\right|^2\right]. \tag{A3}$$

Expanding the equation and moving the expectation through the deterministic variables, we obtain

$$\int_{\lambda_{\min}}^{\lambda_{\max}}\left[r_c^{\,2}(\lambda)-2r_c(\lambda)\sum_{k=1}^{K} w_{c,k}R_k(\lambda)\left(1+\frac{\mathsf{E}[N_k]}{\mathrm{SNR}_k\sigma_{N,k}}\right)\right]\mathrm{d}\lambda+\int_{\lambda_{\min}}^{\lambda_{\max}}\mathsf{E}\left[\left|\sum_{k=1}^{K} w_{c,k}R_k(\lambda)\left(1+\frac{N_k}{\mathrm{SNR}_k\sigma_{N,k}}\right)\right|^2\right]\mathrm{d}\lambda. \tag{A4}$$

To complete the terms in the first integral into a quadratic, we add and subtract

$$\left[\sum_{k=1}^{K} w_{c,k}R_k(\lambda)\left(1+\frac{\mathsf{E}[N_k]}{\mathrm{SNR}_k\sigma_{N,k}}\right)\mathrm{d}\lambda\right]^2,$$

expand the square of summation into multiplication of double summation, and obtain

$$\int_{\lambda_{\min}}^{\lambda_{\max}}\left\{r_c(\lambda)-\sum_{k=1}^{K} w_{c,k}R_k(\lambda)\left(1+\frac{\mathsf{E}[N_k]}{\mathrm{SNR}_k\sigma_{N,k}}\right)\right\}^2\mathrm{d}\lambda+\int_{\lambda_{\min}}^{\lambda_{\max}}\left\{\sum_{k=1}^{K}\sum_{l=1}^{K} w_{c,k}w_{c,l}\,\frac{(\mathsf{E}[N_kN_l]-\mathsf{E}[N_k]\mathsf{E}[N_l])R_k(\lambda)R_l(\lambda)}{\sigma_{N,k}\sigma_{N,l}\mathrm{SNR}_k\mathrm{SNR}_l}\right\}\mathrm{d}\lambda. \tag{A5}$$

Since we assume independence among noise components from different detectors, the term inside the parentheses in the second integral reduces to

$$\left[\sum_{k=1}^{K} w_{c,k}^{\,2}\,\frac{R_k^{\,2}(\lambda)}{\mathrm{SNR}_k^{\,2}}\right], \tag{A6}$$

and the discretized minimization problem then becomes

$$\frac{\Delta\lambda}{L}\sum_{j=1}^{L}\left\{\left[r_c(\lambda_j)-\sum_{k=1}^{K} w_{c,k}R_k(\lambda_j)\left(1+\frac{\mathsf{E}[N_k]}{\mathrm{SNR}_k\sigma_{N,k}}\right)\right]^2+\left[\sum_{k=1}^{K} w_{c,k}^{\,2}\,\frac{R_k^{\,2}(\lambda_j)}{\mathrm{SNR}_k^{\,2}}\right]\right\}. \tag{A7}$$

By invoking the assumption $\mathsf{E}[N_k]=0$ for all k, the above quantity simplifies to

$$\frac{\Delta\lambda}{L}\sum_{j=1}^{L}\left\{r_c^{\,2}(\lambda_j)-2r_c(\lambda_j)\left[\sum_{k=1}^{K} w_{c,k}R_k(\lambda_j)\right]+\left[\sum_{k=1}^{K} w_{c,k}R_k(\lambda_j)\right]^2+\left[\sum_{k=1}^{K} w_{c,k}^{\,2}\,\frac{R_k^{\,2}(\lambda_j)}{\mathrm{SNR}_k^{\,2}}\right]\right\}. \tag{A8}$$

We now differentiate with respect to $w_{c,s}$, set the result to zero, and obtain

$$\sum_{j=1}^{L} r_c(\lambda_j)R_s(\lambda_j)=\sum_{j=1}^{L}\left\{R_s(\lambda_j)\left[\sum_{k=1}^{K} w_{c,k}R_k(\lambda_j)\right]+w_{c,s}\,\frac{R_s^{\,2}(\lambda_j)}{\mathrm{SNR}_s^{\,2}}\right\}. \tag{A9}$$

Moving $R_k(\lambda_j)$ into the summation and interchanging the order of summations, we have

$$\sum_{j=1}^{L} r_c(\lambda_j)R_s(\lambda_j)=\left[\sum_{k=1}^{K} w_{c,k}\sum_{j=1}^{L} R_s(\lambda_j)R_k(\lambda_j)\right]+\frac{w_{c,s}}{\mathrm{SNR}_s^{\,2}}\left[\sum_{j=1}^{L} R_s^{\,2}(\lambda_j)\right]. \tag{A10}$$

Defining $\mathbf{\Pi}_{c,s}\triangleq\mathbf{r}_c{}^T\mathbf{R}_s=\sum_{j=1}^{L} r_c(\lambda_j)R_s(\lambda_j)$, and $\phi_{s,k}\triangleq\mathbf{R}_s{}^T\mathbf{R}_k=\sum_{j=1}^{L} R_s(\lambda_j)R_k(\lambda_j)$, we can write the equation as

$$\mathbf{\Pi}_{c,s}=\left(\sum_{k=1}^{K} w_{c,k}\phi_{s,k}\right)+\frac{w_{c,s}}{\mathrm{SNR}_s^{\,2}}\,\phi_{s,s}. \tag{A11}$$

If we repeat this equation for $s=1,\ldots,K$, we have a linear system of K equations with K unknowns $w_{c,k}$, which can be stated in matrix form as

$$\mathbf{\Pi}_c = \left[\mathbf{A}^T\mathbf{A} + \mathbf{\Phi}\right]\mathbf{w}_c, \tag{A12}$$

where $\mathbf{A}$, $\boldsymbol{\phi}$, and $\mathbf{\Pi}_c$ are defined in Eqs. (13), (14), and (15). From linear algebra, the solution to Eq. (A12) is Eq. (13).

We thank Biliana Paskaleva, Zhipeng Wang, and Amtout Abdenour at the University of New Mexico for many valuable discussions. This work was supported by the National Science Foundation under award IIS-0434102.

References

1. G. Vane and A. F. H. Goetz, "Terrestrial imaging spectroscopy," Remote Sens. Environ. **24,** 1–29 (1988).
2. G. Vane, R. Green, T. Chrien, H. Enmark, E. Hansen, and W. Porter, "The airborne visible infrared imaging spectrometer," Remote Sens. Environ. **44,** 127–143 (1993).
3. R. W. Basedow, D. C. Carmer, and M. E. Anderson, "HYDICE system: implementation and performance," in *Imaging Spectrometry V,* M. R. Descour, J. M. Mooney, D. L. Perry, and L. R. Illing, eds., Proc. SPIE **2480,** 258–267 (1995).
4. T. H. Barnes, "Photodiode array Fourier transform spectrometer with improved dynamic range," Appl. Opt. **24,** 3702–3706 (1985).
5. G. B. Rafert, R. G. Sellar, and L. J. Otten III, "An interactive performance model for spatially modulated Fourier transform spectrometers," in *Imaging Spectrometry,* M. R. Descour, J. M. Mooney, D. L. Perry, and L. R. Illing, eds., Proc. SPIE **2480,** 410–417 (1995).
6. L. J. Otten III, G. B. Rafert, and R. G. Sellar, "The design of an airborne Fourier transform visible hyperspectral imaging system for light aircraft environmental remote sensing," in *Imaging Spectrometry,* M. R. Descour, J. M. Mooney, D. L. Perry, and L. R. Illing, eds., Proc. SPIE **2480,** 418–424 (1995).
7. L. J. Otten III, A. D. Meigs, A. Franklin, R. D. Sears, M. W. Robinson, J. B. Rafert, and D. S. Fronterhouse, "On board spectral imager data processor," in *Imaging Spectrometry V,* M. R. Descour and S. S. Shen, eds., Proc. SPIE **3753,** 86–94 (1995).
8. J. S. Tyo and T. S. Turner, "Variable retardance, Fourier transform imaging spectropolarimeters for visible spectrum remote sensing," Appl. Opt. **40,** 1450–1458 (2001).
9. W. R. Bell, "Multispectral Thermal Imager—overview," in *Algorithms for Multispectral, Hyperspectral, and Ultraspectral Imagery VII,* S. S. Shen and M. R. Descour, eds., Proc. SPIE **4381,** 173–183 (2001).
10. U. Sakoglu, J. S. Tyo, M. M. Hayat, S. Raghavan, and S. Krishna, "Spectrally adaptive infrared photodetectors with bias-tunable quantum dots," J. Opt. Soc. Am. B **21,** 7–17 (2004).
11. H. J. Caulfield, "Artificial color," Neurocomputing **51,** 463–465 (2003).
12. P. Bhattacharya, S. Krishna, J. D. Phillips, D. Klotzkin, and P. J. McCann, "Quantum dot carrier dynamics and far infrared devices," in *Optoelectronics Materials and Devices II,* Y.-K. Su and P. Bhattacharya, eds., Proc. SPIE **4078,** 84–89 (2000).
13. P. Bhattacharya, S. Krishna, J. Phillips, P. J. McCann, and K. Namjou, "Carrier dynamics in self-organized quantum dots and their application to long-wavelength sources and detectors," J. Cryst. Growth **227,** 27–35 (2001).
14. S. Krishna, P. Rotella, S. Raghavan, A. Stintz, M. M. Hayat, J. S. Tyo, and S. W. Kennerly, "Bias-dependent tunable response of normal incidence long wave infrared quantum-dot photodetectors," in *Proceedings of the IEEE/LEOS Annual Meeting* (Institute of Electrical and Electronics Engineers, 2002) Vol. 2, pp. 754–755.
15. S. Krishna, "Quantum dots-in-a-well infrared photodetectors," J. Phys. D **38,** 2142–2150 (2005).
16. U. Sakoglu, Z. Wang, M. M. Hayat, J. S. Tyo, S. Annamalai, P. Dowd, and S. Krishna, "Quantum dot detectors for infrared sensing: bias-controlled spectral tuning and matched filtering," in *Nanosensing: Materials and Devices,* M. Saif Islam and A. K. Dutta, eds., Proc. SPIE **5593,** 396–407 (2004).
17. Z. Wang, U. Sakoglu, S. Annamalai, N.-R. Weisse-Bernstein, P. Dowd, J. S. Tyo, M. M. Hayat, and S. Krishna, "Real-time implementation of spectral matched filtering algorithms using adaptive focal plane array technology," in *Imaging Spectrometry X,* A. G. Tescher, ed., Proc. SPIE **5546,** 73–83 (2004).
18. Z. Wang, B. Paskaleva, J. S. Tyo, and M. M. Hayat, "Canonical correlations analysis for assessing the performance of adaptive spectral imagers," in *Defense and Security Symposium, Algorithms and Technologies for Multispectral, Hyperspectral, and Ultraspectral Imagery XI,* S. S. Shen and P. E. Lewis, eds., Proc. SPIE **5806,** 23–34 (2005).
19. Z. Wang, B. Paskaleva, M. M. Hayat, and J. S. Tyo, "Analyzing spectral sensors with highly overlapping bands," presented at the Twelfth SPIE Defense and Security Symposium on Algorithms and Technologies for Multispectral, Hyperspectral, and Ultraspectral Imagery, Orlando, Fla., 18–20 April 2006.
20. B. Paskaleva, M. M. Hayat, M. M. Moya, and R. J. Fogler, "Multispectral rock type separation and classification," in *Infrared Spaceborne Remote Sensing XII,* M. Strojnik, ed., Proc. SPIE **5543,** 152–163 (2004).
21. B. Paskaleva and M. M. Hayat, "Optimized algorithm for spectral band selection for rock-type classification," in *Defense and Security Symposium, Algorithms and Technologies for Multispectral, Hyperspectral, and Ultraspectral Imagery XI,* S. S. Shen and P. E. Lewis, eds., Proc. SPIE **5806,** 131–138 (2005).
22. B. Paskaleva, M. M. Hayat, S. Tyo, Z. Wang, and M. Martinez, "Feature selection for spectral sensors with overlapping noisy spectral bands," presented at the Twelfth SPIE Defense and Security Symposium on Algorithms and Technologies for Multispectral, Hyperspectral, and Ultraspectral Imagery, Orlando, Fla., 18–20 April 2006.
23. V. Ryzhii, "Physical model and analysis of quantum-dot infrared photodetectors with blocking layer," J. Appl. Phys. **89,** 5117–5124 (2001).
24. P. Bhattacharya, *Semiconductor Optoelectronic Devices,* 2nd ed. (Prentice-Hall, 1996).
25. E. L. Dereniak and G. D. Boreman, *Infrared Detectors and Systems* (Wiley, 1996).
26. H. Stark and J. Woods, *Probability and Random Processes with Applications to Signal Processing,* 3rd ed. (Prentice-Hall, 2002).
27. S. Krishna, D. Forman, S. Annamalai, P. Dowd, P. Varangis, T. Tumolillo, Jr., A. Gray, J. Zilko, K. Sun, M. Liu, J. Campbell, and D. Carothers, "Demonstration of a 320 × 256 two-color focal plane array using InAs/InGaAs quantum dots in well detectors," Appl. Phys. Lett. **86,** 193501–3 (2005).
28. B. F. Levine, "Quantum-well infrared photodetectors," J. Appl. Phys. **74,** R1–R81 (1993).
29. J. Phillips, P. Bhattacharya, S. W. Kennerly, D. W. Beekman, and M. Dutta, "Self-assembled InAs-GaAs quantum-dot intersubband detectors," IEEE J. Quantum Electron. **35,** 936–942 (1999).
30. F. F. Sabins, *Remote Sensing: Principles and Interpretation,* 3rd ed. (Freeman, 1997).